Journal of Applied Physics

Lock-in carrierography non-destructive imaging of silicon wafers and silicon solar cells

Cite as: J. Appl. Phys. **128**, 180903 (2020); https://doi.org/10.1063/5.0022852
Submitted: 10 August 2020 . Accepted: 16 October 2020 . Published Online: 09 November 2020

Peng Song, Feng Yang, Junyan Liu, and Andreas Mandelis

COLLECTIONS

This paper was selected as Featured

View Online Export Citation CrossMark

ARTICLES YOU MAY BE INTERESTED IN

Nanoscale ultrasonic subsurface imaging with atomic force microscopy
Journal of Applied Physics **128**, 180901 (2020); https://doi.org/10.1063/5.0019042

Photothermal approach for cultural heritage research
Journal of Applied Physics **128**, 180904 (2020); https://doi.org/10.1063/5.0023432

Semiconducting metal oxides empowered by graphene and its derivatives: Progresses and critical perspective on selected functional applications
Journal of Applied Physics **128**, 180905 (2020); https://doi.org/10.1063/5.0021826

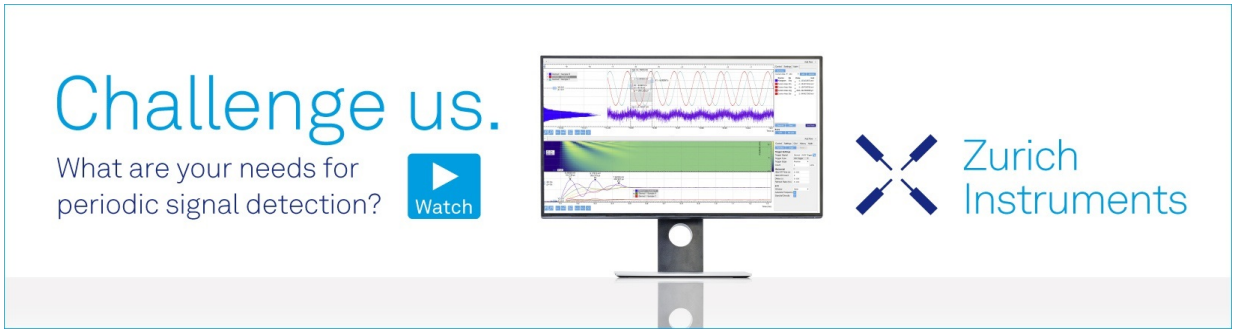

© 2020 Author(s).

Journal of Applied Physics | PERSPECTIVE | scitation.org/journal/jap

Lock-in carrierography non-destructive imaging of silicon wafers and silicon solar cells

Cite as: J. Appl. Phys. **128**, 180903 (2020); doi: 10.1063/5.0022852
Submitted: 10 August 2020 · Accepted: 16 October 2020 ·
Published Online: 9 November 2020

View Online Export Citation CrossMark

Peng Song,[1] Feng Yang,[2] Junyan Liu,[2,3,a)] and Andreas Mandelis[4,a)]

AFFILIATIONS

[1]School of Instrumentation Science and Engineering, Harbin Institute of Technology, Harbin 150001, China
[2]School of Mechatronics Engineering, Harbin Institute of Technology, Harbin 150001, China
[3]State Key Laboratory of Robotics and System, Harbin Institute of Technology, Harbin 150001, China
[4]Center for Advanced Diffusion-Wave and Photoacoustic Technologies (CADIPT), University of Toronto, Toronto M5S 3G8, Canada

[a)]**Authors to whom correspondence should be addressed:** ljywlj@hit.edu.cn and mandelis@mie.utoronto.ca

ABSTRACT

Carrier transport and electrical properties are relevant to the performance of semiconductor materials and photovoltaic devices. In recent years, various kinds of high-resolution luminescence-based methods have been proposed to image these properties. Lock-in carrierography (LIC), as a dynamic photoluminescence-based method, has the advantages of self-calibration, higher signal to noise ratio than dc or transient modalities, and high-frequency imaging ability. At the present stage of development, LIC has evolved into homodyne lock-in carrierography and heterodyne lock-in carrierography. In this Perspective, we discuss the principles and theoretical background of both LIC modalities and review experimental systems and methods. In addition, we also provide a brief overview of key LIC applications and future outlook.

Published under license by AIP Publishing. https://doi.org/10.1063/5.0022852

I. INTRODUCTION

The silicon wafer-based photovoltaic (PV) share of ca. 95% of the total PV device production in 2017 is a strong indicator of Si dominance in the solar cell technology sector.[1] Manufacturing characterization methods of silicon wafers and solar cells play an important role in improving cell efficiency and reducing cost in the PV market. In the latest decades, optical imaging methodologies including lock-in thermography,[2,3] light beam-induced current (LBIC),[4] and luminescence-based imaging methods[5,6] were developed for spatially resolved characterization of the carrier transport properties (such as carrier lifetime, diffusion coefficient, and surface recombination velocities) and electrical properties (such as photogenerated current, open-circuit voltage, fill factor, series resistance, shunt resistance, and conversion efficiency) of silicon wafers and solar cells.[7,8]

Luminescence imaging as a method of detection of radiative recombination photons emitted from p-n junctions was proposed by Uchida since 1963.[9] Compared with other methods, luminescence imaging measurements are not affected by minority carrier trapping or by artifacts caused by excess carriers in space charge regions. Following decades of development, luminescence based phenomena can be classified as electroluminescence (EL)[5] and photoluminescence (PL)[6] in terms of carrier excitation sources. EL and PL imaging are fast nondestructive methodologies which have been widely used for the determination of spatially resolved effective diffusion length,[10,11] junction voltage,[12] saturation current density,[13] series resistance,[14–18] shunt,[19–21] and efficiency[22] of silicon solar cells. However, EL can only be used with finished solar cells, whereas PL excited by photons is possible to monitor the processing of solar cells at any stage of fabrication.[23,24] Thus, much attention has been paid to this latter advanced spatially resolved characterization method.

For the conversion of PL intensity under steady-state conditions (in arbitrary units) into absolute carrier lifetimes, a reliable calibration procedure is always required.[25] On the other hand, compared with steady-state PL, dynamic PL imaging techniques which include transient (time-resolved) PL,[26] quasi-steady-state PL,[27,28] and lock-in PL/carrierography[29] [a camera-based imaging extension of photocarrier radiometry (PCR)[30]] feature calibration-free and contactless characterization.

Published under license by AIP Publishing.

Lock-in carrierography (LIC) is a frequency-domain PL imaging methodology which combines the digital lock-in algorithm with the PL imaging method. After a decade of development, it has evolved into two complementary branches: homodyne lock-in carrierography (HoLIC) and heterodyne lock-in carrierography (HeLIC), for spatially resolved characterization of carrier transport and electrical properties of silicon wafers and solar cells. The advantage of HeLIC in producing high-frequency images overcomes the limitations of today's low-frame-rate cameras and opens up a wide frequency range of optoelectronic process diagnostics which are difficult or impossible to detect under steady and quasi-steady conditions. In this Perspective article, the aforementioned LIC advantages and features will be reviewed in detail with respect to theory, experimental configurations, and applications and placed in perspective of conventional PL-based methodologies with emphasis on quantitative optoelectronic imaging.

II. THEORY

A. Carrier density waves

Carrier density waves (CDWs, harmonically excited and modulated free minority carrier densities) form the basis for the quantitative determination of photocarrier transport and electrical properties. Analytical equations for CDWs for silicon wafers and solar cells will be presented in this section. The space and time dependence of minority carrier density $\Delta n(\mathbf{r},t)$ in a silicon wafer is governed by the carrier continuity equation as follows:

$$\frac{\partial \Delta n(\mathbf{r}, t)}{\partial t} = G(\mathbf{r}, t) - \frac{\Delta n(\mathbf{r}, t)}{\tau_b} + D\nabla^2 \Delta n(\mathbf{r}, t), \tag{1}$$

where G is the carrier generation rate, τ_b is the bulk lifetime, and D is the diffusion coefficient.

Assuming the laser spot size is much larger than the carrier diffusion length, i.e., lateral invariance, Eq. (1) can be further treated as a depth-resolved equation in the one-dimensional limit for thin wafers and solar cells.

B. Carrier density waves in a silicon wafer

The carrier density within a silicon wafer excited by intensity-modulated illumination follows a diffusion-wave behavior.[31] A one-dimensional single layer model of a silicon wafer excited by an intensity-modulated laser is shown in Fig. 1.

Minority carrier transport properties (bulk lifetime, diffusion coefficient, and surface recombination velocities) are also indicated in Fig. 1. For this geometry, Eq. (1) can be written as

$$D\frac{\partial^2 \Delta n(z, t)}{\partial z^2} - \frac{\Delta n(z, t)}{\tau_b} - \frac{\partial \Delta n(z, t)}{\partial t} = -G_0 \beta e^{-\beta z} g(t), \tag{2}$$

where $G_0 = I_0(1-R)/h\nu$ is the carrier generation rate (I_0 is the illumination intensity, R is the reflectivity, $h\nu$ the single photon energy), β is the optical absorption coefficient, and $g(t)$ is the modulation function.

After Fourier transformation, the time-domain equation [Eq. (2)] can be converted into the frequency-domain carrier-density-wave equation,

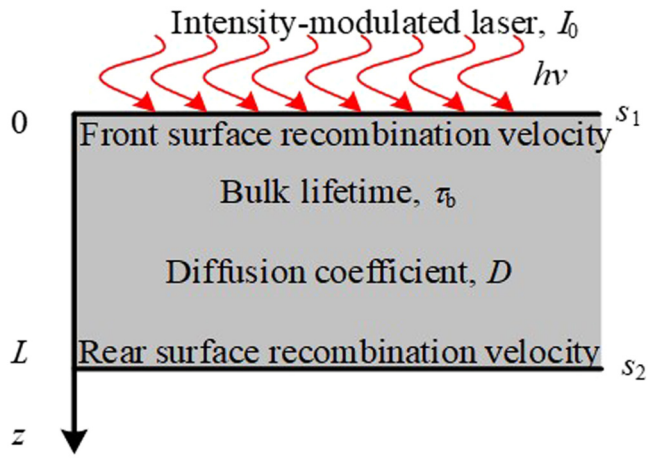

FIG. 1. Schematic of the one-layer silicon wafer model.

$$\frac{d^2 \Delta n(z, \omega)}{dz^2} - \sigma^2 \Delta n(z, \omega) = \frac{-G_0 \beta}{D} e^{-\beta z}, \tag{3a}$$

where $\omega = 2\pi f$ is the modulation angular frequency, f is the modulation frequency, and

$$\sigma(\omega) = 1/L_{ac}(\omega) = \left[(\tau_b^{-1} + i\omega)/D\right]^{1/2} \tag{3b}$$

is the complex wavenumber with ac carrier diffusion length L_{ac}. From this expression, it can be seen that the carrier diffusion length decreases with increasing modulation frequency, which is similar to thermal wave behavior and lock-in thermography[32] in the limit of $\omega \gg \tau_b^{-1}$. To the best of our knowledge, based on this parametric dependence of the LIC signals, this modality is the only method allowing the major carrier transport properties to be resolved through appropriate measurements.

The general solution of Eq. (3a) can be written as

$$\Delta n(z, \omega) = C_1 e^{-\sigma z} + C_2 e^{-\sigma(L-z)} - \frac{G_0 \beta}{D(\beta^2 - \sigma^2)} e^{-\beta z}, \tag{4}$$

where C_1, C_2 are integration constants which are determined through the boundary conditions

$$\begin{cases} D\left.\dfrac{d\Delta n(\omega, z)}{dz}\right|_{z=0} = s_1 \Delta n(\omega, z = 0), \\ D\left.\dfrac{d\Delta n(\omega, z)}{dz}\right|_{z=L} = -s_2 \Delta n(\omega, z = L), \end{cases} \tag{5}$$

where L is the wafer thickness. The carrier density, i.e., the solution to Eq. (3), under sine-wave excitation and square-wave excitation can be found in Refs. 31 and 33, respectively.

Published under license by AIP Publishing.

C. Carrier density waves within silicon solar cells

A schematic diagram for a solar cell with an abrupt p-n junction is shown in Fig. 2. In this figure, the geometry of the solar cell contains an n-type region, a p-type region, and a depletion layer (space charge region, SCR). The n- and p-region thicknesses are d and l, respectively, while the finite thickness of the SCR is neglected in this case. The minority carrier transport properties are also shown in Fig. 2.

The carrier continuity equations for the n- and p-regions of the solar cell can be written as

$$\begin{cases} D_p \dfrac{\partial^2 \Delta p(z,t)}{\partial z^2} - \dfrac{\Delta p(z,t)}{\tau_p} - \dfrac{\partial \Delta p(z,t)}{\partial t} = -G_0 \beta e^{-\beta(z+d)} g(t), & -d \le z \le 0, \\ D_n \dfrac{\partial^2 \Delta n(z,t)}{\partial z^2} - \dfrac{\Delta n(z,t)}{\tau_n} - \dfrac{\partial \Delta n(z,t)}{\partial t} = -G_0 \beta e^{-\beta(z+d)} g(t), & 0 < z \le l. \end{cases} \tag{6}$$

After Fourier transformation, one obtains

$$\begin{cases} \dfrac{d^2 \Delta p(z,\omega)}{dz^2} - \sigma_p^2 \Delta p(z,\omega) = \dfrac{-G_0 \beta}{D_p} e^{-\beta(z+d)}, & -d \le z \le 0, \\ \dfrac{d^2 \Delta n(z,\omega)}{dz^2} - \sigma_n^2 \Delta n(z,\omega) = \dfrac{-G_0 \beta}{D_n} e^{-\beta(z+d)}, & 0 < z \le l. \end{cases} \tag{7}$$

where $\sigma_j = [(\tau_j^{-1} + i\omega)/D_j]^{1/2}$ is the respective complex wavenumber. The subscripts p and n represent holes and electrons, respectively. The general solution of Eq. (7) yields the expressions

$$\begin{cases} \Delta p(z,\omega) = C_{p1}\cosh(-\sigma_p z) + C_{p2}\sinh[-\sigma_p z] + a_p e^{-\beta(z+d)}, & -d \le z \le 0, \\ \Delta n(z,\omega) = C_{n1}\cosh[-\sigma_n z] + C_{n2}\sinh[-\sigma_n z] + a_n e^{-\beta(z+d)}, & 0 < z \le l, \end{cases} \tag{8}$$

where C_{p1}, C_{p2}, a_p, C_{n1}, C_{n2}, and a_n are determined by the following boundary conditions:[34]

$$\begin{cases} D_p \dfrac{\partial \Delta p(z,\omega)}{\partial z}\Big|_{z=-d} = s_1 \Delta p(z,\omega)\big|_{z=-d}, \\ D_n \dfrac{\partial \Delta n(z,\omega)}{\partial z}\Big|_{z=l} = -s_2 \Delta n(z,\omega)\big|_{z=l}, \end{cases} \tag{9a}$$

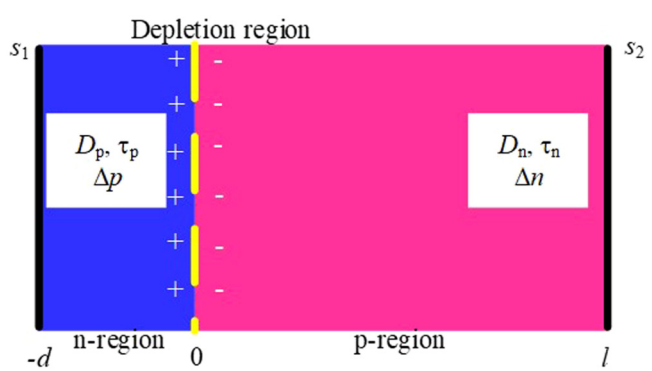

FIG. 2. Schematic of the 1D two-layer structure model for a solar cell.

$$\begin{cases} \Delta n(z,\omega)\big|_{z=0} = n_0[e^{\frac{qV}{k_B T}} - 1]\big|_{z=0}, \\ \Delta p(z,\omega)\big|_{z=0} = p_0[e^{\frac{qV}{k_B T}} - 1]\big|_{z=0}. \end{cases} \tag{9b}$$

Here, n_0 and p_0 are the equilibrium electron and hole concentrations, respectively, and V is the SCR electrostatic potential.

D. Lock-in carrierography (LIC)

As mentioned above, LIC as a frequency-domain PL imaging method has evolved into homodyne lock-in carrierography (HoLIC) and heterodyne lock-in carrierography (HeLIC). HoLIC akin to the time-domain PL imaging method detects the fundamental frequency term, while HeLIC detects the beat term of two closely spaced frequencies. The latter modality was mainly developed to overcome the current state-of-the-art near-infrared cameras, which feature low frame rates (around 100 Hz max) that cannot directly achieve the high frequency (10 kHz–100 kHz +) modulation required to resolve optoelectronic transport parameters.

E. Homodyne LIC (HoLIC)

The frequency-domain HoLIC signal $S_{\mathrm{ho}}(z,\omega)$ is proportional to the excess carrier concentration

$$S(z,\omega) \approx C\Delta n(z,\omega)[\Delta n(z,\omega) + N_{\mathrm{d}}], \tag{10}$$

where C is a proportionality factor, N_{d} is the doping concentration, and the modulated excess CDW $\Delta n(z,\omega)$ is described by the

Published under license by AIP Publishing.

following expression:

$$\Delta n(z, \omega) = \Delta n_0(z) + A(z, \omega)\cos[\omega t + \varphi(z, \omega)], \tag{11}$$

with amplitude $A(z,\omega)$ and phase $\varphi(z,\omega)$ of the photogenerated carrier density wave, and dc component $\Delta n_0(z)$. The proportionality factor C incorporates all the frequency-independent factors into account, such as the radiative recombination coefficient, the sample reflectivity, the collection efficiency, and the quantum efficiency of the camera. Inserting Eq. (11) into Eq. (10) yields the expression

$$S(z, \omega) \approx C\{\Delta n_0^2(z) + [2\Delta n_0(z) + N_\mathrm{d}]A\cos(\omega t + \varphi) + \Delta n_0(z)N_\mathrm{d} + A^2\cos^2(\omega t + \varphi)\}. \tag{12}$$

From Eq. (12), the PL signal generated using modulated-intensity illumination includes dc, fundamental, and higher harmonic terms.

In the HoLIC mode, only the fundamental frequency component survives the digital lock-in filter algorithm. Thus, the frequency-domain HoLIC signal at depth z can be expressed as

$$S_\mathrm{Ho}(\omega, z) \approx C[2\Delta n_0(z) + N_\mathrm{d}]A\cos[\omega t + \varphi(z, \omega)] = C[2\Delta n_0(z) + N_\mathrm{d}]\Delta N(z, \omega). \tag{13}$$

Equation (13) indicates that the HoLIC signal depends on the dc component $\Delta n_0(z)$, the doping concentration N_d, and the ac component $\Delta N(z,\omega)$. In the low injection limit, $Dn_0(z) \ll N_d$, the HoLIC signal is linear with the excitation. Furthermore, HoLIC images can only be generated at low modulation frequencies using the current state-of-the-art near-infrared cameras, which feature low frame rates (around 100 Hz).

F. Heterodyne LIC (HeLIC)

In the heterodyne mode, two angular frequencies ω_1 and ω_2 with equal illumination intensities are mixed. The excess carrier density becomes

$$\Delta n(z, t) = 2\Delta n_0(z) + A(z, \omega_1)\cos[\omega_1 t + \varphi(z, \omega_1)] + A(z, \omega_2)\cos[\omega_2 t + \varphi(z, \omega_2)]. \tag{14}$$

Inserting Eq. (14) into Eq. (10) yields the following expression for the product of the carrier density waves on the rhs at a fixed depth z:

$$\begin{aligned}\Delta n[\Delta n + N_\mathrm{d}] = {} & (4\Delta n_0^2 + 2N_\mathrm{d}\Delta n_0) + (4\Delta n_0 + N_\mathrm{d})A(\omega_1, \varphi_1)\cos(\omega_1 t + \varphi_1) + (4\Delta n_0 + N_\mathrm{d})A(\omega_2, \varphi_2)\cos(\omega_2 t + \varphi_2) \\ & + \{ A^2(\omega_1, \varphi_1)\cos[2(\omega_1 t + \varphi_1)]\} /2 + \{ A^2(\omega_2, \varphi_2)\cos[2(\omega_2 t + \varphi_2)]\} /2 + 2A(\omega_1, \varphi_1)A(\omega_2, \varphi_2)\cos[(\omega_2\text{-}\omega_1)t \\ & + (\varphi_2 - \varphi_1)] + A^2(\omega_1, \varphi_1)/2 + 2A(\omega_1, \varphi_1)A(\omega_2, \varphi_2)\cos[(\omega_2 + \omega_1)t + (\varphi_2 + \varphi_1)] + A^2(\omega_2, \varphi_2)/2.\end{aligned} \tag{15}$$

It is seen from Eq. (15) that the mixed signal has a dc term, fundamental frequency terms (f_1 and f_2), second harmonic terms ($2f_1$ and $2f_2$), a beat frequency term ($|f_1_f_2|$), and a sum frequency term (f_1+f_2). For heterodyne signals, lock-in detection with a reference signal at the beat frequency can only retain the beat frequency term.

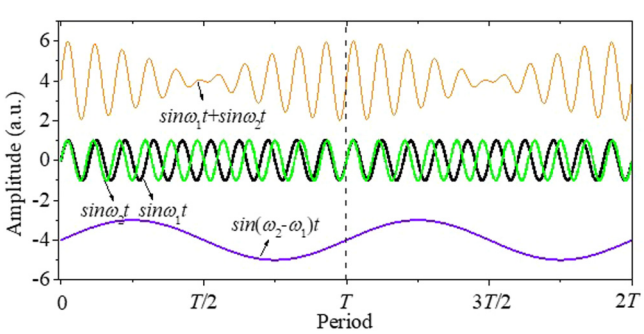

FIG. 3. Modulated signals at various frequencies generated by the heterodyne mixing process.

For better understanding the signal mixing process, the modulation signal components $\sin(2\pi f_1 t)$, $\sin(2\pi f_2 t)$, $\sin(2\pi|f_1_f_2|t)$, and $\sin(2\pi f_1 t)$+$\sin(2\pi f_1 t)$ are shown in Fig. 3. It can be seen that the beat frequency signal which only depends on $|f_1_f_2|$ has the lowest modulation frequency envelope, which can be easily captured by the camera's low frame-rate.

When a simulated lock-in process (mixer and low-pass filter) was applied to all four signals with lock-in reference set at the beat frequency, the demodulated amplitudes of these signals were all zero except for the beat frequency signal. This confirms that there are no additional beat frequency components in $\sin(2\pi f_1 t)$, $\sin(2\pi f_2 t)$, and the mixed signal resulting from $\sin(2\pi f_1 t)$+$\sin(2\pi f_1 t)$. The beat frequency term generated in Eq. (15) is non-zero by virtue of the $\Delta n(z, \omega)[\Delta n(z, \omega) + N_d]$ product structure of the HeLIC signal.[33]

The heterodyne signal at depth z can thus be expressed as

$$\begin{aligned}S_\mathrm{He}(z, \Delta\omega) &= A(z; \omega_1, \varphi_1)A(z; \omega_2, \varphi_1)\cos[(\omega_2 - \omega_1)t + (\varphi_2 - \varphi_1)] \\ &= A(z; \omega_1, \varphi_1)e^{-i\varphi_1}A(z; \omega_2, \varphi_1)e^{i\varphi_2} \\ &= \Delta n(z, -\omega_1)\Delta n(z, \omega_2),\end{aligned} \tag{16}$$

where $\Delta\omega$=$|\omega_1 - \omega_2|$ is the angular beat frequency.

Published under license by AIP Publishing.

After performing an integration over the thickness of a wafer or a solar cell, one can get the homodyne and heterodyne signal $S_{Ho/He}$, and thus the amplitude and phase of the homodyne signal and heterodyne signal can be expressed as

$$\begin{cases} A_{Ho/He}(\omega) = \sqrt{\mathrm{Re}(S_{Ho/He})^2 + \mathrm{Im}(S_{Ho/He})^2}, \\ \varphi_{Ho/He}(\omega) = -\tan^{-1}(\frac{\mathrm{Im}(S_{Ho/He})}{\mathrm{Re}(S_{Ho/He})}). \end{cases} \tag{17}$$

Combining Eqs. (16) and (17), the carrier transport properties can be obtained by best fitting these equations to experimental amplitude- and phase-frequency dependencies. It is worth mentioning that the heterodyne amplitude is the only effective signal channel for HeLIC. This is so because the phase across all frequencies is always close to 0° due to the small difference in values between f_1 and f_2.

III. INSTRUMENTATION AND EXPERIMENTAL LIC CONFIGURATIONS

A description of a typical experimental LIC setup can be found elsewhere[38] and a schematic of such a setup combined with a PCR probe is shown in Fig. 4.

Two 808-nm diode lasers were intensity-modulated with frequencies f_1 and f_2 using a two-channel function generator. Intensity-scan or frequency-scan experiments can be realized by adjusting the signals from this function generator fed into the laser drivers. The laser beams were collimated, homogenized, and spread by a microlens array across the sample surface with intensity variations less than 5%. InGaAs detector I was used to monitor the laser intensity. A neutral density filter was placed in front of detector I. An InGaAs camera (bandwidth: 0.9 ~ 1.7 mm) with 640 × 512 pixels was used for HeLIC and HoLIC imaging from the sample. A data acquisition card was employed to generate reference and camera-trigger signals. As shown in Fig. 4, the frequency of the reference signal is $f = f_1 = f_2$ in the HoLIC mode, while in the HeLIC mode, the frequency is Δf. A digital lock-in algorithm with external triggering of the camera was implemented for LIC.[35] A single-element PCR system was used simultaneously with the LIC system for signal consistency cross-checking and quantitative studies. A lock-in amplifier demodulated the PCR signal at frequency f_1, f_2, or Δf. Long-pass filters were mounted in front of the camera and detector II to eliminate the reflected laser beam. The camera and the two single-element-detectors recorded signals simultaneously. The sample was placed on a water cooled plate so as to maintain a stable temperature.

In summary, the foregoing system has the following features: (1) LIC and PCR experiments can be realized simultaneously for cross-checking and quantitative consistency; (2) intensity-scan and frequency-scan experiments can be carried out for the determination of various properties which will be discussed in Sec. IV.

IV. APPLICATIONS

A. Semiconductor materials and substrates

1. Effective lifetimes

Effective lifetime (τ_{eff}) information, which is generally affected by both bulk lifetime and surface recombination, is relevant for semiconductor materials and photovoltaic diagnostics. Homodyne lock-in carrierography was successfully applied to effective lifetime imaging of silicon wafers.[36] In contrast to most other effective lifetime measurement techniques, HoLIC, as a diffusion-wave methodology, carries phase (φ_{ho}) information in addition to signal amplitude which is directly related to the effective lifetime of optoelectronic materials and devices, $\varphi_{ho} = -\tan(\omega\tau_{eff})$, and thus features self-consistency, self-calibration, and enhanced measurement reliability.[36] Additionally, the effective lifetime obtained by HoLIC is independent of the angular frequency during the frequency-scanning process.[37]

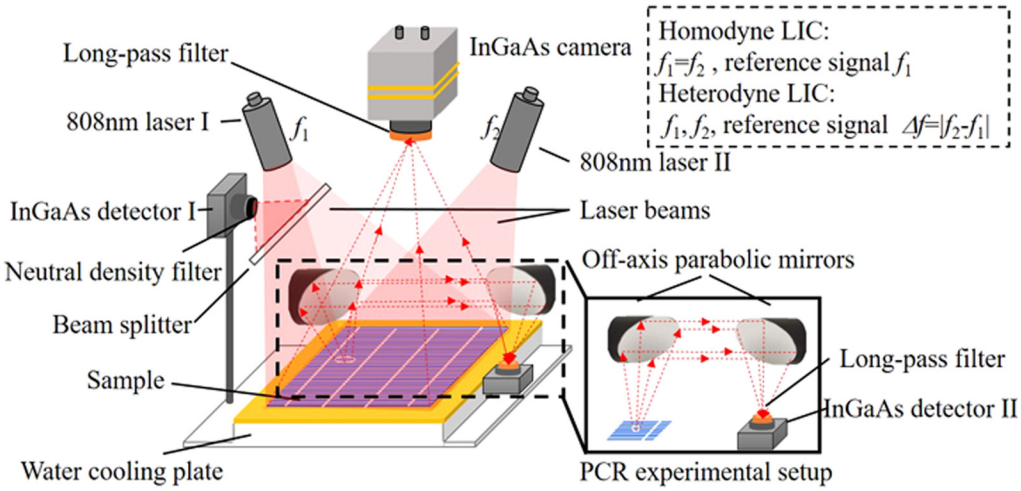

FIG. 4. Schematic of the LIC experimental setup combined with photocarrier radiometry.

Published under license by AIP Publishing.

2. Dopant concentrations

Doping determines the resistivity and effective lifetime in a silicon wafer. As Eqs. (10) and (13) show, the PL signal is not only determined by the excess minority carrier concentration Δn, but also by the dopant concentration N_d. If one is able to extract $\Delta n(t)$ from PL signals at various injection levels, the dopant concentration may also be determined simply by carrying out an intensity-scanned HoLIC experiment. As discussed above, the effective lifetime can be derived from the HoLIC phase channel directly at various carrier injection levels. The minority carrier concentration can be estimated if the generation rate and effective lifetime are known. Then, the intensity-scanned HoLIC amplitudes at various minority carrier concentrations can be fitted to the theory to extract the dopant concentration and thus the resistivity. A procedure for determining dopant concentration and resistivity of an n-type Si wafer with both surfaces partly passivated with amorphous-Si(α-Si) is shown in Fig. 5.[38] Figures 5(a) and 5(b) show the dependences of amplitude and phase on laser intensity at point A on the wafer, respectively. Furthermore, the dependence of the effective lifetime on the intensity can be obtained from the measurement shown in Fig. 5(b). As shown in Fig. 5(c), the lifetime is not a constant but varies with the laser intensity (rigorously speaking, excess carrier concentration). This phenomenon was also confirmed by quasi-steady-state photoconductance (QSSPC) which is a well-established and standard effective lifetime measurement technique.[39]

The inset dopant concentration and resistivity images obtained using LIC are shown in Figs. 5(d) and 5(e), respectively. The doping inhomogeneity can be observed in Fig. 5(d). Moreover, as shown in Fig. 5(e), the values of the LIC-derived resistivity were in good agreement with those measured independently using the conventional four-point probe method. Although a series of intensity-scanned LIC measurements must be done to extract the dopant concentration image, for wafer fabrication process monitoring, this procedure is expected to take less than 1 min to complete the whole measurement by automatic laser intensity changes and has the potential for in-line quality control.

3. Transport property imaging of silicon wafers

Spatially resolved changes of carrier transport properties in silicon wafers (i.e., bulk lifetime, diffusion coefficient, and front and rear surface recombination velocities) are more important than averaged quality measurements and thus surface and bulk quality imaging characterization methods are increasingly in demand, especially since the size of state-of-the-art wafers has already reached 450 mm. As the expression for the ac carrier diffusion length shows, the carrier diffusion length varies with modulation frequency which is akin to the thermal-wave diffusion length and

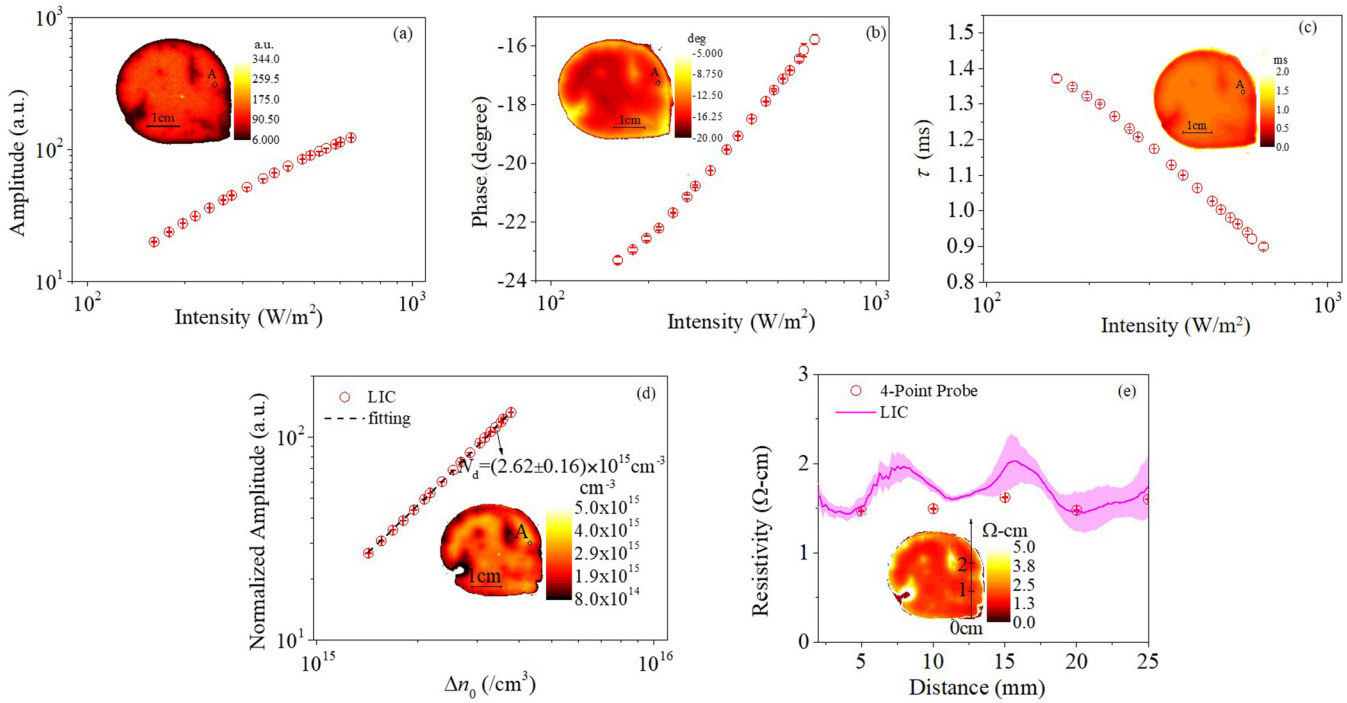

FIG. 5. (a) Laser intensity dependence of amplitude and (b) phase, and (c) effective lifetime at a selected position (point A). (d) Dependence of normalized amplitude on photocarrier concentration and the corresponding best-fitted curves. (e) Resistivity profile comparison between LIC and four-point probe along the vertical lines at 0 cm. Modulation frequency: 50 Hz. The inset images are (a) amplitude, (b) phase, (c) lifetime at 649 W/m^2, (d) the best-fitted N_d, and (e) resistivity. Reproduced (adapted) with permission from Song *et al.*, Semicond. Sci. Technol. 33, 12LT01 (2018). Copyright 2018 IOP Publishing Ltd.

Published under license by AIP Publishing.

can be used to perform 3D parameter reconstructions.[31,40] It is thus concluded that LIC has the ability to resolve the carrier transport properties from the lumped effective lifetime at high enough modulation frequencies ($\omega\tau_{eff} \gg 1$).[31]

Photocarrier radiometry imaging has been used for imaging the major carrier transport properties of a wafer.[30,41] It can achieve high resolution but can be time-consuming as point-by-point scanning always takes substantial amounts of time for measuring an entire wafer surface. To greatly speed up the measurement efficiency and enable dynamic parameter monitoring which requires modulation frequencies that are too high (>10 kHz) compared to the maximum frame rate of commercial NIR cameras, heterodyne lock-in carrierography (HeLIC) has been developed.[42,43] A theoretical HeLIC model has been established and artificial scratches on the front and rear surfaces of a wafer have been observed using HeLIC imaging contrast.[33] HeLIC imaging of the surface recombination velocity (SRV) of wet-cleaned Si wafers was also reported and is shown in Fig. 6. The measurement time for obtaining an SRV image was reduced to 3 min. SRV values from 0.1 to 100 m/s could be measured under the assumptions of fixed bulk lifetime and known diffusion coefficient.[44]

One of the main issues for HeLIC measurements is to identify the uniqueness range of simultaneous determination of the major carrier transport parameters of Si wafers, because the heterodyne amplitude is the only effective signal channel for HeLIC unlike HoLIC which also features a phase channel. Simulations were carried out to explore the value ranges of HeLIC-determined unique bulk lifetimes and/or SRVs from calculated data with added random noise.[45] The results indicated that either bulk lifetime or surface lifetime (a function of SRV) can only be resolved if the values of these two parameters are very different, while the diffusion coefficient can be resolved in all cases. An extended range of simultaneously determined unique transport parameters can be attained by reducing the unknown parameters, such as by assuming the same surface recombination velocity at the front and rear surfaces,[44–46] or by assuming a homogeneous diffusion coefficient image,[44,46] and/or a homogeneous bulk lifetime image.[45,46] The validity of any of these assumptions can be reliably verified from homodyne photocarrier radiometry through measurements of both amplitude and phase channels.

The effective lifetime can be estimated once the carrier transport properties are determined and the thickness of a wafer is known.[47] Figure 7 shows the comparison of the effective lifetime of a silicon wafer, 290-μm thick, by micro-photoconductance (μ-PCD), homodyne photocarrier radiometry (HoPCR), heterodyne photocarrier radiometry (HePCR), and heterodyne lock-in carrierography (HeLIC) under the same injection excess carrier concentration ($\Delta n = 6 \times 10^{15}/\text{cm}^3$). It is obvious that there is good measurement consistency among all these techniques.

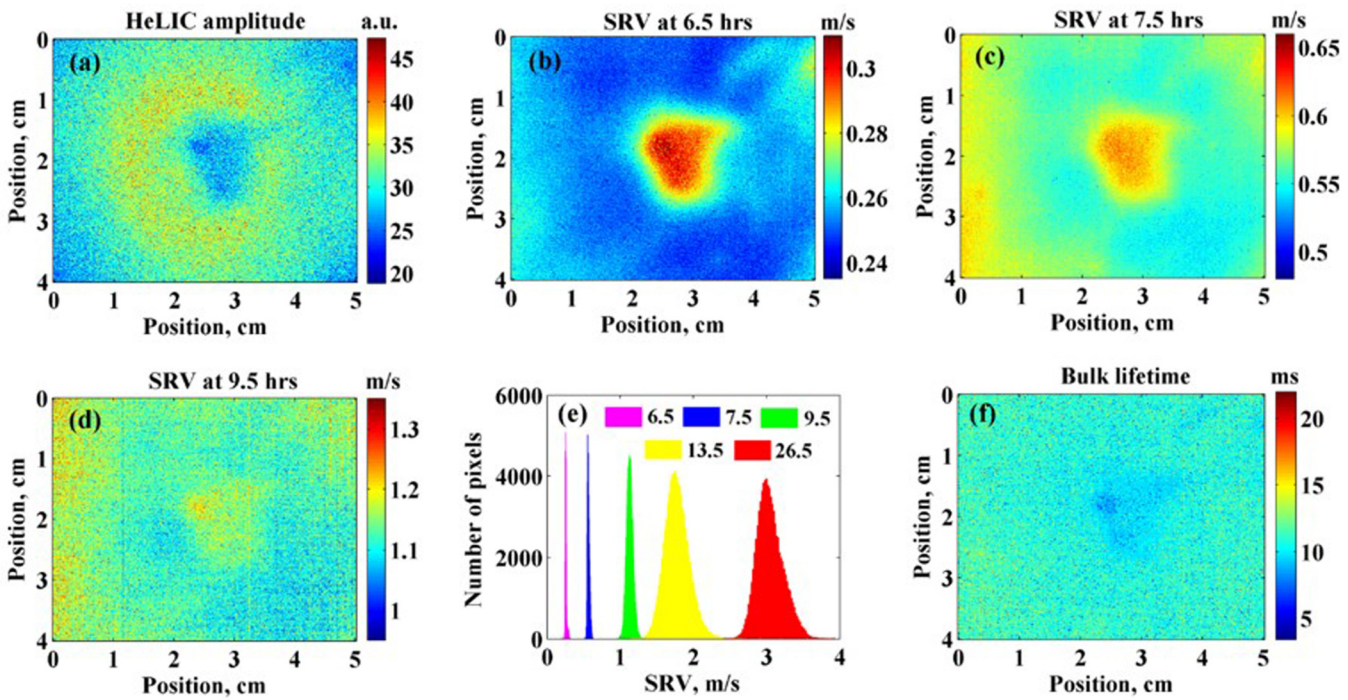

FIG. 6. (a) HeLIC amplitude image at 100 Hz (raw image, no uniformity or smoothing corrections); (b)–(d) SRV images at various queue-times; (e) pixel-value statistical distributions of SRV images at various queue-times (h); and (f) bulk lifetime image.[44]

Published under license by AIP Publishing.

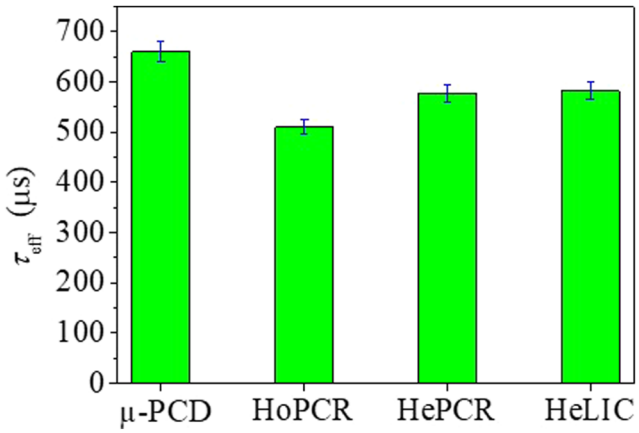

FIG. 7. Effective lifetime of a silicon wafer with 1 Ω-cm resistivity estimated by μ-PCD, HoPCR, HePCR, and HeLIC under the same injection carrier concentration.

B. Photovoltaics

1. Transport property imaging

Carrier transport properties determine the electrical parameters of a solar cell, such as the saturation current density and open-circuit voltage. With the rapid development of mc-Si solar cell technologies, spatially resolved characterization of carrier transport properties and electrical parameters is necessary for process monitoring and module quality control. Imaging of carrier transport properties (base minority carrier lifetime, diffusion coefficient, and front and rear surface recombination velocities) of a mc-Si solar cell at open-circuit conditions has been demonstrated using photocarrier radiometry imaging (PCR point-by-point mapping).[48] To improve the detection efficiency, HeLIC has been used to quantitatively image the base minority carrier lifetime of mc-solar cells.[49,50]

2. Electrical properties

Solar cell luminescence-based methods generate signals related to diode voltage and thus allow the quantitative evaluation of the spatially resolved electrical properties. HoLIC amplitude and phase channels have been linked to the voltage; furthermore, the conversion efficiency of solar cells based on an optoelectronic diode expression,[51,52]

$$J(V) = J_{SC}(V_{\hbar\omega_i}) - J_0(V)\left[\exp\left(\frac{qV}{k_B T}\right) - 1\right] - J_{NR}, \qquad (18)$$

where $J(V)$ represents the current density at junction voltage V of a diode, $J_{SC}(V_{\hbar\omega i})$ is the short-current density generated by the incident photons, J_0 is the saturation current density, k_BT/q is the thermal voltage (0.026 V at 300 K), and J_{NR} is the current density caused by the emission and absorption processes with energies $E_{NR} = \hbar\omega_{NR}$.[51]

A series of LIC amplitude images under different working conditions was taken and used to simultaneously extract the images of photo-generated current density, saturation diode current density, ideality factor, photovoltage at maximum power point,[53] and conversion efficiency[54] of a mc-Si solar cell, which were in good agreement with results from lock-in thermography and electrical measurements (Fig. 8).

Based on the photocarrier radiative recombination current flux relation [Eq. (18)],[51] imaging of key electrical parameters (photogenerated current density, open circuit voltage, and maximum power voltage) of a mc-Si solar cell has been measured using LIC in a contactless manner.[55] This non-contacting characterization approach allows the measurement of I–V equivalent characteristics of solar cells at all stages of fabrication, thereby extending the conventional electrical I–V measurements to earlier phases of the production process, identifying manufacturing problems, and

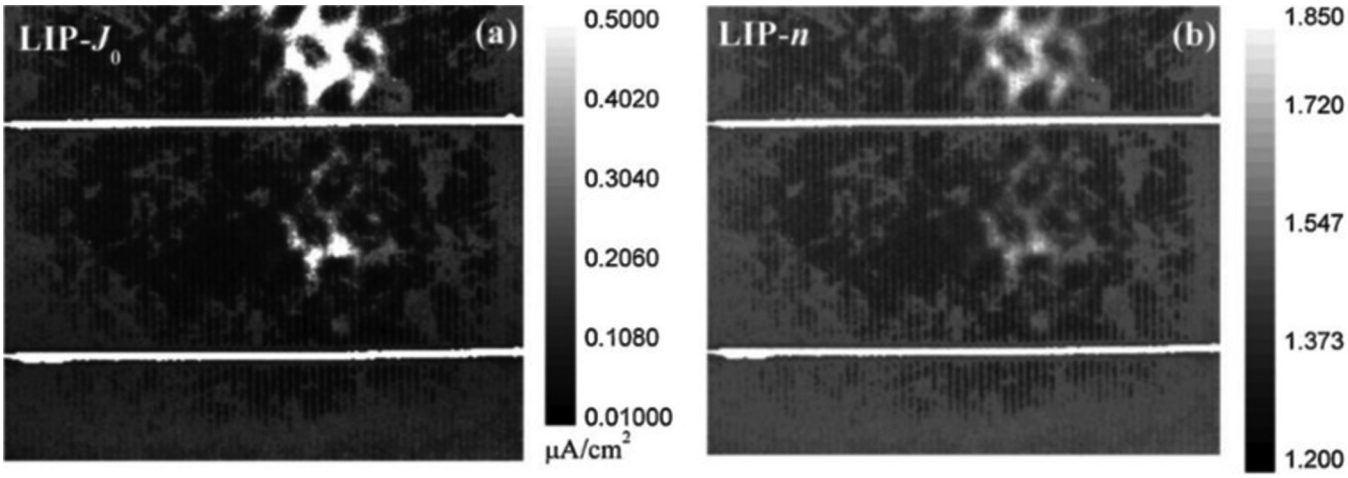

FIG. 8. Saturation diode current density J_0 and ideality factor n images using LIC (or lock-in PL: LIP) at 10 Hz (a) LIP-J_0 and (b) LIP-n image, illumination power density: 0.038 W cm^{-2}. Reproduced with permission from Liu *et al.*, Phys. Status Solidi A 210(10), 2135 (2013). Copyright 2013 Wiley-VCH Verlag GmbH & Co. KGaA.

Published under license by AIP Publishing.

preventing them from being carried on to the entire production line, only to surface at the device completion stage when it is typically too late to fix the manufacturing process.

Besides the aforementioned electrical parameters, series resistance can also be quantified from luminescence images as it causes lateral variations in diode voltage under operating conditions. A LIC-based modulation method has been introduced to automatically eliminate diffusion-limited carriers during a lock-in process.[56] The spatially resolved series resistances of a mc-Si solar cell and a c-Si solar cell using LIC were found to be in good agreement with those measured using steady-state (dc) PL. LIC has the advantage of high signal-to-noise ratio and is independent of acquisition

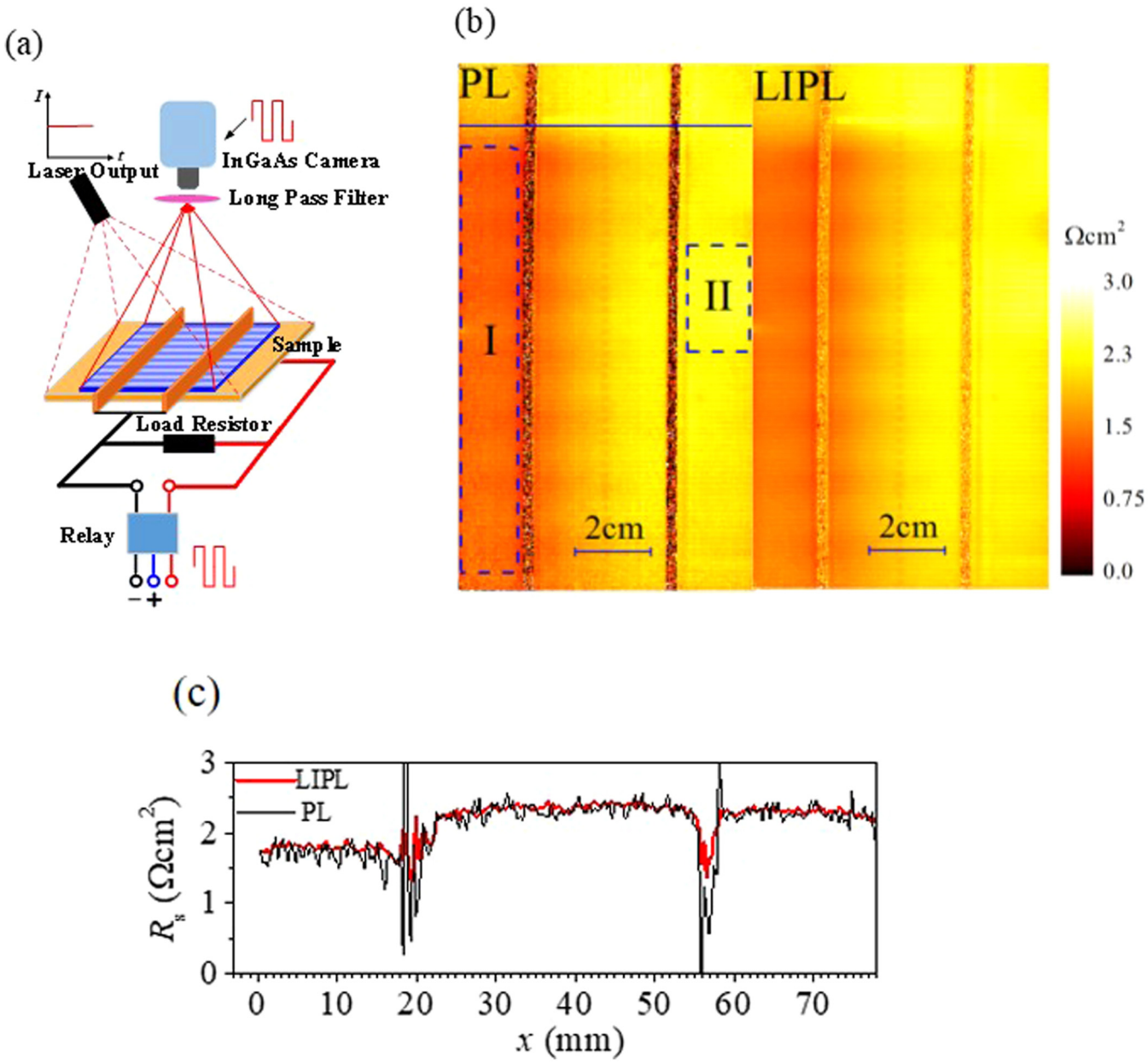

FIG. 9. Series resistance images of a mc-Si solar cell derived using PL and lock-in PL (LIPL or LIC). (a) A schematic of the LIPL experimental setup, (b) PL-R_s image and LIPL-R_s image, (c) R_s measured using PL and LIPL along the horizontal line marked in (b). The total PL (LIPL) acquisition time was 320 s (160 s). Reproduced with permission from Song *et al.*, Phys. Status Solidi RRL 11(7), 1700153 (2017). Copyright 2017 Wiley-VCH Verlag GmbH & Co. KGaA.

Published under license by AIP Publishing.

time.[56] Figure 9 shows a schematic of the LIC experimental setup and comparison results between LIC and PL. In another application, by virtue of its high SNR advantage, the LIC imaging modality was successfully used to spatially determine the saturation current density and series resistance of a solar cell irradiated by 1 MeV electron beams[57] and to identify the different types of broken fingers in a solar cell.[58]

V. COMPARISONS AND PERSPECTIVE AMONG STATE-OF-THE-ART PL SEMICONDUCTOR CHARACTERIZATION METHODS

Lock-in carrierography as a dynamic photoluminescence imaging method, mainly features:

(1) *Self-calibration and imaging.* This compares favorably with the separate calibration required for the steady-state PL method to quantitatively characterize the performance of semiconductors: A series of calibration approaches has been demonstrated including quasi-steady state PL[59–61] which correlates imaging data with non-spatially resolved data from quasi-steady-state photoconductance. In contrast, no calibration process is need for LIC imaging: One can directly obtain the effective lifetime from the LIC phase channel.[36] Furthermore, no prior information about carrier mobility or dopant concentration is required.
(2) *High signal-to-noise ratio.* Through the use of digital lock-in algorithms, the LIC SNR is higher than the steady-state PL imaging method. Figure 10 shows a comparison between LIC and PL signals from a Si solar cell irradiated by 1 MeV electron beams with the same camera profile setting and with the same acquisition time. It is seen that LIC can clearly distinguish the background and effective region of the irradiated solar cell, while in PL imaging, the noise has effectively buried the effective PL signal. In conclusion, LIC is a promising tool for semiconductor and solar cell characterization for many applications, including space module powering.
(3) *Separation capability of bulk and surface properties.* LIC, as a dynamic diffusion-wave based technique,[31] has the virtue of *depth selectivity* thereby being able to simultaneously image surface recombination velocity and bulk lifetime in semiconductor materials.[44–46] Compared to steady-state PL imaging methods, including PL spectroscopy, LIC imaging is less complicated as there are no requirements for spectrally selective low-pass, high-pass or band-pass filters,[10] or multi-wavelength excitation[62] for the determination of bulk and surface properties.
(4) *High frequency imaging ability.* A key advantage of HeLIC is that it overcomes today's low frame-rate (100-Hz) camera limitations to access millisecond to submicrosecond physical processes dynamically. This allows imaging of fast kinetic optoelectronic events in novel nanoscale semiconductor materials and devices such as colloidal quantum dot solar cells with ns-scale lifetimes.[63,64]

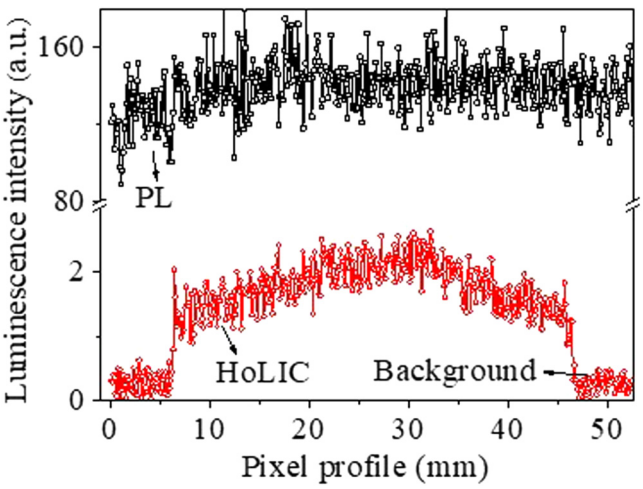

FIG. 10. Comparison of LIC and PL results for a solar cell irradiated by 1 MeV electron beams.

VI. CONCLUSIONS AND OUTLOOK

The advent of expensive large-area silicon wafers and the modern day electronic industry's requirements for high-conversion-efficiency silicon solar cells has placed stringent demands on improved quality control and corresponding process monitoring tools. PL-based methods are perfectly suitable for in-line monitoring across the entire semiconductor and photovoltaic device chain due to their contactless non-destructive nature. Lock-in carrierography, as a state-of-the-art dynamic modulated PL imaging modality, has evolved into homodyne and heterodyne lock-in carrierography with a multitude of tested applications and a very promising future. In this perspective, the principles and theoretical background of both LIC modalities and experimental systems have been discussed and the recent applications of LIC on silicon wafers and solar cells summarized.

In the field of Si wafer characterization, LIC has been used successfully for quantitative imaging of effective lifetime, dopant concentration, and carrier transport properties. In the field of photovoltaics, it can be used for non-contact imaging of carrier transport properties and electrical parameters (photogeneration current density, photo-generated current density, saturation diode current density, ideality factor, series resistance, and conversion efficiency) at any and all stages of the device fabrication process. With these wide applications in silicon technologies, LIC has exhibited depth-selectivity, high SNR, and dynamic transport property imaging capabilities. Despite significant progress, there is still plenty of room for further improvements and applications of LIC to Si technology and beyond as a nondestructive characterization imaging metrology standard.

First, LIC must predictably, uniquely, reliably, and accurately determine the carrier transport parameters of silicon wafers and/or silicon solar cells. These attributes are essential for establishing LIC as a fabrication process control and device modeling in Si and other semiconductor technologies. During the LIC characterization process, multi-parameter fitting of theoretical signal formulations to frequency scanned data is required to simultaneously obtain the

Published under license by AIP Publishing.

carrier transport properties. Although uniqueness range optimization of photocarrier transport parameter measurements of silicon wafers using combined quantitative heterodyne lock-in carrierography imaging and photocarrier radiometry has been carried out,[45] a detailed reliability analysis using sensitivity coefficient maps[65] for uniqueness determination of transport parameters of solar cells using homodyne and heterodyne lock-in carrierography is still lacking.

Second, the acquisition of quantitative images of physical properties of silicon solar cells such as temperature coefficient[66] and carrier transport properties (bulk lifetime, diffusion coefficient, front and rear surface recombination velocities) at arbitrary working conditions using LIC is still under development. We expect HeLIC-derived quantitative transport property images acquired at times fast enough for real-time device fabrication to materialize in the near future, both with the adaptation of the simplified HeLIC theory to best-fitting complete sets of frequency scanned images from silicon solar cells, and with the further development of fast near-infrared cameras to access sub-microsecond dynamic photocarrier kinetics/dynamics.

Third, with the rapid development of third generation photovoltaics such as perovskite solar cells and quantum dot solar cells, the instability mechanisms of these solar cells against thermal, moisture, oxygen, and photonic disturbances are still unclear.[67] LIC constitutes a promising tool for identifying such instability mechanisms in combination with other techniques, specifically PCR and mid-infrared thermography, with the latter providing the important complementary nonradiative CDW recombination information to the radiative pathway provided by PCR and LIC.

In view of the foregoing features, attributes and advantages of LIC, one can reasonably expect further growth in LIC applications in a wide range of electronic quality control, non-destructive evaluation, and parameter measurements in technologies involving space solar cells under cosmic radiation, in next generation novel semiconductor materials and nanoscale semiconductors and in-line process control leading to manufacturing process optimization.

ACKNOWLEDGMENTS

J.L. and P.S. acknowledge the National Natural Science Foundation of China (NNSFC) (Grant No. 61571153). P.S. also acknowledges the Project funded by the China Postdoctoral Science Foundation (Grant No. 2020M670902). A.M. is grateful to the Natural Sciences and Engineering Research Council of Canada (NSERC) for a Discovery grant.

DATA AVAILABILITY

The data that support the findings of this study are available from the corresponding author upon reasonable request.

REFERENCES

[1]See www.ise.fraunhofer.de for more information about">www.ise.fraunhofer.de for more information about Photovoltaics Report, Fraunhofer ISE, Freiburg, Germany (2019).
[2]F. Frühauf and O. Breitenstein, Sol. Energy Mater. Sol. Cells **169**, 195 (2017).
[3]O. Breitenstein, Sol. Energy Mater. Sol. Cells **93**, 2933 (2011).
[4]M. Padilla, B. Michl, B. Thaidigsmann, W. Warta, and M. C. Schubert, Sol. Energy Mater. Sol. Cells **120**, 282 (2014).
[5]T. Fuyuki, H. Kondo, T. Yamazaki, Y. Takahashi, and Y. Uraoka, Appl. Phys. Lett. **86**, 262108 (2005).
[6]T. Trupke, R. A. Bardos, M. C. Schubert, and W. Warta, Appl. Phys. Lett. **89**, 044107 (2006).
[7]Z. Hameiri and P. Chaturvedi, Appl. Phys. Lett. **102**, 073502 (2013).
[8]W. Kwapil, S. Wasmer, A. Fell, J. M. Greulich, and M. C. Schubert, Sol. Energy Mater. Sol. Cells **191**, 71 (2019).
[9]I. Uchida, Jpn. J. Appl. Phys. **2**, 561 (1963).
[10]P. Würfel, T. Trupke, T. Puzzer, E. Schäffer, W. Warta, and S. W. Glunz, J. Appl. Phys. **101**, 123110 (2007).
[11]J. A. Giesecke, M. Kasemann, and W. Warta, J. Appl. Phys. **106**, 014907 (2009).
[12]M. Glatthaar, J. Haunschild, R. Zeidler, M. Demant, J. Greulich, B. Michl, W. Warta, S. Rein, and R. Preu, J. Appl. Phys. **108**, 014501 (2010).
[13]M. Glatthaar, J. Giesecke, M. Kasemann, J. Haunschild, M. The, W. Warta, and S. Rein , J. Appl. Phys. **105**, 113110 (2009).
[14]D. Hinken, K. Ramspeck, K. Bothe, B. Fischer, and R. Brendel, Appl. Phys. Lett. **91**, 182104 (2007).
[15]J. Haunschild, M. Glatthaar, M. Kasemann, S. Rein, and E. R. Weber, Phys. Status Solidi RRL **3**(7–8), 227 (2009).
[16]T. Trupke, E. Pink, R. A. Bardos, and M. D. Abbottet, Appl. Phys. Lett. **90**, 093506 (2007).
[17]H. Kampwerth, T. Trupke, J. W. Weber, and Y. Augarten, Appl. Phys. Lett. **93**, 202102 (2008).
[18]M. Glatthaar, J. Haunschild, M. Kasemann, J. Giesecke, W. Warta, and S. Rein, Phys. Status Solidi RRL **4**(1–2), 13 (2010).
[19]O. Breitenstein, J. Bauer, T. Trupke, and R. A. Bardos, Prog. Photovolt. Res. Appl. **16**, 325 (2008).
[20]M. Kasemann, D. Grote, B. Walter, W. Kwapil, T. Trupke, Y. Augarten, R. A. Bardos, E. Pink, M. D. Abbott, and W. Warta, Prog. Photovolt. Res. Appl. **16**, 297 (2008).
[21]Y. Augarten, T. Trupke, M. Lenio, J. Bauer, J. W. Weber, M. Juhl, M. Kasemann, and O. Breitenstein, Prog. Photovolt. Res. Appl. **21**, 933 (2013).
[22]C. Shen, M. A. Green, O. Breitenstein, T. Trupke, M. Zhang, and H. Kampwerth, Sol. Energy Mater. Sol. Cells **123**, 41 (2014).
[23]K. Bothe and D. Hinken, "Quantitative luminescence characterization of crystalline silicon solar cells," in *Semiconductors and Semimetals* (Elsevier, 2013), Chap. V, pp. 259–339.
[24]J. A. Giesecke, M. C. Schubert, F. Schindler, and W. Warta, IEEE J. Photovolt. **5**(1), 313 (2015).
[25]S. Herlufsen, J. Schmidt, D. Hinken, K. Bothe, and R. Brendel, Phys. Status Solidi RRL **2**, 245 (2008).
[26]D. Kiliani, A. Herguth, G. Micard, J. Ebser, and G. Hahn, Sol. Energy Mater. Sol. Cells **106**, 55 (2012).
[27]J. A. Giesecke, M. C. Schubert, D. Walter, and W. Warta, Appl. Phys. Lett. **97**, 092109 (2010).
[28]S. Herlufsen, K. Ramspeck, D. Hinken, A. Schmidt, J. Müller, K. Bothe, J. Schmidt, and R. Brendel, Phys. Status Solidi RRL **5**, 25 (2011).
[29]A. Melnikov, A. Mandelis, J. Tolev, P. Chen, and S. Huq, J. Appl. Phys. **107**, 114513 (2010).
[30]A. Mandelis, J. Batista, and D. Shaughnessy, Phys. Rev. B **67**, 205208 (2003).
[31]A. Mandelis, *Diffusion-Wave Fields Mathematical Methods and Green Functions* (Springer, New York, 2001), Chap. 9.
[32]O. Breitenstein, H. Straube, and K. Iwig, Sol. Energy Mater. Sol. Cells **185**, 66 (2018).
[33]Q. Sun, A. Melnikov, and A. Mandelis, Phys. Status Solidi A **213**(2), 405 (2016).
[34]A. Mandelis, J. Appl. Phys. **66**, 5572 (1989).
[35]O. Breitenstein, W. Warta, and M. C. Schubert, *Lock-In Thermography: Basics and Use for Evaluating Electronic Devices and Materials* (Springer, 2018).
[36]Q. M. Sun, A. Melnikov, and A. Mandelis, Appl. Phys. Lett. **101**, 242107 (2012).
[37]Q. M. Sun, A. Melnikov, J. Wang, and A. Mandelis, J. Phys. D Appl. Phys. **51**, 15LT01 (2018).

Published under license by AIP Publishing.

[38]P. Song, A. Melnikov, Q. Sun, A. Mandelis, and J. Liu, Semicond. Sci. Technol. **33**, 12LT01 (2018).
[39]R. A. Sinton, A. Cuevas, M. Stuckings, "Quasi-steady-state photoconductance: A new method for solar cell material and device characterization," *Proceedings of 25th IEEE Photovoltaic Specialists Conference* (IEEE, Washington, 1996), p. 457.
[40]Ch. Schmidta, F. Altmanna, and O. Breitenstein, Mater. Sci. Eng. B **177**(12), 1261 (2012).
[41]J. Liu, P. Song, L. Qin, F. Wang, and Y. Wang, Acta Phys. Sin. **64**, 087804 (2015) (in Chinese).
[42]A. Melnikov, P. Chen, Y. Zhang, and A. Mandelis, Int. J. Thermophys. **33**, 2095 (2012).
[43]Q. M. Sun, A. Melnikov, and A. Mandelis, Int. J. Thermophys. **36**, 1274 (2015).
[44]Q. Sun, A. Melnikov, A. Mandelis, and R. H. Pagliaro, Appl. Phys. Lett. **112**, 012105 (2018).
[45]P. Song, A. Melnikov, Q. Sun, A. Mandelis, and J. Liu, J. Appl. Phys. **125**, 065701 (2019).
[46]P. Song, A. Melnikov, Q. Sun, R. H. Pagliaro, X. Sun, J. Liu, and A. Mandelis, Semicond. Sci. Technol. **35**, 055013 (2020).
[47]See https://pveducation.org/pvcdrom/characterisation/surface-recombination for surface recombination for surface recombination.
[48]P. Song, J. Liu, H. Xu, and Y. Wang, Int. J. Thermophys. **39**, 119 (2018).
[49]Q. M. Sun, A. Melnikov, and A. Mandelis, "Quantitative heterodyne lock-in carrierographic imaging of silicon wafers and solar cells," *IEEE 44th Photovoltaic Specialist Conference (PVSC)* (IEEE, Washington, 2014), p. 1860
[50]Q. M. Sun, A. Melnikov, and A. Mandelis, Int. J. Thermophys. **37**, 45 (2016).
[51]A. Mandelis, Y. Zhang, and A. Melnikov, J. Appl. Phys. **112**, 054505 (2012).
[52]M. Glatthaar, J. Haunschild, R. Zeidler, M. Demant, J. Greulich, B. Michl, W. Warta, S. Rein, and R. Preu, J. Appl. Phys. **108**, 014501 (2010).
[53]J. Liu, A. Melnikov, and A. Mandelis, Phys. Status Solidi A **210**(10), 2135 (2013).
[54]J. Liu, A. Melnikov, and A. Mandelis, Int. J. Thermophys. **36**, 987 (2015).
[55]J. Liu, A. Melnikov, and A. Mandelis, J. Appl. Phys. **114**, 104509 (2013).
[56]P. Song, J. Liu, M. Oliullah, and Y. Wang, Phys. Status Solidi RRL **11**(7), 1700153 (2017).
[57]P. Song, J. Liu, H. Xu, and Y. Wang, Int. J. Thermophys. **39**, 128 (2018).
[58]P. Xiao, P. Song, J. Liu, and X. Sun, Int. J. Thermophys. **41**, 54 (2020).
[59]J. A. Giesecke, M. C. Schubert, and W. Warta, Phys. Status Solidi A **209**, 2286 (2012).
[60]J. A. Giesecke, B. Michl, F. Schindler, M. C. Schubert, and W. Warta, Sol. Energy Mater. Sol. Cells **95**, 197 (2011).
[61]J. A. Giesecke, M. C. Schubert, B. Michl, F. Schindler, and W. Warta, Sol. Energy Mater. Sol. Cells **95**, 1011 (2011).
[62]L. Sirleto, A. Irace, G. F. Vitale, L. Zeni, and A. Cutolo, Opt. Lasers Eng. **38**, 461 (2002).
[63]L. Hu, A. Mandelis, and Q. Sun, IEEE J. Photovolt. **9**(1), 132 (2019).
[64]L. Hu, M. Liu, A. Mandelis, Q. Sun, A. Melnikov, and E. H. Sargent, Sol. Energy Mater. Sol. Cells **174**, 405 (2018).
[65]X. Guo, A. Mandelis, J. Tolev, and K. Tang, J. Appl. Phys. **121**, 095101 (2017).
[66]R. Eberle, S. T. Haag, I. Geisemeyer, M. Padilla, and M. C. Schubert, "Temperature coefficient imaging for silicon solar cells," IEEE J. Photovolt. **8**(4), 930 (2018).
[67]Y. Wu, H. Wei, L. Xu, B. Cao, and H. Zeng, J. Appl. Phys. **128**, 050903 (2020).

Published under license by AIP Publishing.